Check for updates

RESEARCH ARTICLE

ADVANCED MATERIALS INTERFACES Open Access

www.advmatinterfaces.de

Water Nanofilms Mediate Adhesion and Heat Transfer at Hematite-Hydrocarbon Interfaces

Fionn Carman, Fernando Bresme, Billy Wu, Daniele Dini, and James P. Ewen*

A detailed understanding of nanoscale heat transport at metal oxide-hydrocarbon interfaces is critical for many applications that require efficient thermal management. Under ambient conditions, water nanofilms are expected to form at these interfaces, but these are rarely accounted for in simulations. Using molecular dynamics simulations, it is shown that water nanofilms at the hydroxylated hematite/poly-α-olefin (PAO) interface significantly affect wettability and thermal transport. Including water nanofilms improves agreement with experimental work of adhesion, which cannot be replicated with anhydrous systems using realistic solid–liquid interactions. For water films thicker than one monolayer, interfacial thermal resistance (ITR) converges to a consistent value, independent of solid–liquid interaction strength. This value is dominated by the ITR at the water/PAO interface. The ITR at the water/PAO interface is dependent on the surface area between the water film and the PAO and the magnitude of the interfacial potential. These simulations provide a more precise estimate of ITR at the hematite/PAO interface by accounting for surface hydration expected in experiments under ambient conditions. This study offers crucial insights into the roles of surface hydroxylation and water nanofilms in controlling wettability and thermal transport at industrially important interfaces.

1. Introduction

Understanding heat transfer at solid-liquid interfaces is important for biosensing,[1] lubrication,[2,3] and thermal management in components such as batteries,[4] motors,[5] and electronic devices.[6] Efficient heat transfer ensures optimal performance, prevents overheating, and extends the operational lifespan of these systems. The interfacial thermal resistance (ITR) quantifies the resistance to heat flow over an interface and is given by the equation:[7]

$$R_k = \frac{\Delta T}{J_q} \tag{1}$$

where R_k is the ITR, ΔT is the temperature discontinuity at the interface and J_q is the heat flux normal to the plane of the interface. Minimizing the ITR is essential to improve thermal management in various applications, particularly those involving micro or nanoscale components.[7,8]

Nanoscale heat transfer at metal oxide-hydrocarbon interfaces is of high importance for applications including cooling fluids[9,10] and lubricants.[2,11] However, the ITR has rarely been quantified for interfaces relevant to these applications either through experiments or molecular simulations. In a recent study,[12] we investigated the ITR between a hematite surface, α-Fe_2O_3(0001), and a hydrocarbon fluid, poly-α-olefin (PAO), using non-equilibrium molecular dynamics (NEMD) simulations. Our model was designed to mimic the interface between the steel battery casing and the dielectric fluid inside battery immersion cooling systems.[10] The outer oxidation layer of steel will be mostly α-Fe_2O_3 at ambient temperatures[13] and the (0001) facet is the most thermodynamically stable.[14] The α-Fe_2O_3(0001)/PAO interface is also important for understanding the thermal properties of oil-based iron oxide nanofluids.[15] We evaluated various solid–liquid Lennard–Jones interaction potentials,[16–18] which gave a wide range of ITR values (R_k = 4-21 K m^2 GW^{-1}).[12] Stronger interfacial interactions gave reduced ITR and increased the fluid density close to the surface.[12] To identify the most accurate solid-liquid interaction potential for our system, we compared the work of adhesion determined using the dry-surface method,[19] to that calculated from the experimental contact angle of PAO4 on steel.[20] Here, the 4 refers to the kinematic viscosity of PAO in cSt at 100 °C. The comparison revealed that the existing hematite-hydrocarbon potentials overestimated the work of adhesion from experiments.[12] When the strength of the solid-liquid potential was further reduced to

F. Carman, D. Dini, J. P. Ewen
Department of Mechanical Engineering
South Kensington Campus, Imperial College London
London SW7 2AZ, UK
E-mail: fionn.carman18@imperial.ac.uk

F. Bresme
Department of Chemistry, Molecular Sciences Research Hub
Imperial College London
London W12 0BZ, UK

B. Wu
Dyson School of Design Engineering
South Kensington Campus, Imperial College London
London SW7 2AZ, UK

The ORCID identification number(s) for the author(s) of this article can be found under https://doi.org/10.1002/admi.202500267

© 2025 The Author(s). Advanced Materials Interfaces published by Wiley-VCH GmbH. This is an open access article under the terms of the Creative Commons Attribution License, which permits use, distribution and reproduction in any medium, provided the original work is properly cited.

DOI: 10.1002/admi.202500267

match the experimental work of adhesion, the ITR increased substantially ($R_k = 33$ K m^2 GW^{-1}).[12] This value of the ITR is similar to that measured experimentally for the gold-hexadecane interface ($R_k = 36$ K m^2 GW^{-1}).[21] The observed discrepancy between the experimental and simulation work of adhesion using state-of-the-art solid-liquid interatomic potentials[18] suggests that the metal oxide/hydrocarbon interface modeled in the simulation differs from the experimental one. In our previous study,[12] a dry hematite surface was assumed to be directly in contact with the PAO4 fluid. However, in experimental systems, thin water films are known to form on the surface of metal oxides when the surfaces are exposed to air.[22] Adsorbed water molecules can also partially dissociate, forming covalently bonded hydroxyl groups on the oxide surface.[22] Anhydrous α-Fe_2O_3(0001) is hydrophobic, but surface hydroxylation makes the surface hydrophilic due to surface-water hydrogen bond interactions.[23] Ambient pressure X-ray photoelectron spectroscopy (XPS) studies revealed surface hydroxylation on the α-Fe_2O_3(0001) surface at very low relative humidity (RH) ~10^{-7} % at 295 K.[24] Full surface hydroxylation occurs at RH values of around 5%.[24] In this study, we are targeting these experimental conditions, corresponding to full surface hydroxylation. At higher humidities, the onset of water adsorption was observed, with the coverage reaching 1 water monolayer (ML) thickness (10 molecules nm^{-2}) at 15% RH, increasing to 1.5 ML at 34% RH.[24] At very high humidity (~ 95% RH), hematite nanoparticles can stabilize water nanofilms of up to 4–5 ML at 298 K.[25] The hydrophobicity of hematite can be restored by heating the hydroxylated surface to 60 °C, which is sufficient to remove the surface hydroxyls and surface-bound water layers.[23]

The wettability of hydrocarbons or other non-polar fluids on oxide surfaces, such as silica,[26] alumina,[26] quartz,[27] sapphire,[27] and mica,[28] can be affected by thin interfacial water layers. Depending on the relative hydrophilicity/oleophilicity of the surface and the temperature, interfacial water droplets or films can be formed.[28,29] The interfacial water molecules disrupt the hydrocarbon-surface interactions, making the surface more oleophobic than the dry surface.[28] The effect of thin water films on the solid-liquid work of adhesion, W_{sl}, can be understood by combining Young's equation with the Young–Dupré equation to obtain W_{sl} in terms of the contact angle, θ, and the liquid–vapor surface tension, γ_{lv}:[30]

$$W_{sl} = \gamma_{lv}(1 + \cos\theta) \quad (2)$$

Thus, the W_{sl} decreases as θ increases. The experimental steel/water contact angle ($\theta_{sw} = 66.2°$) gives $W_{sl} = 101.0$ mJ m^{-2}, which is higher than the steel/PAO4 $W_{sl} = 57.5$ mJ m^{-2},[20] despite the lower contact angle ($\theta_{sp} = 10.9°$). It should be noted that the contact angles of steel and other surfaces are quite sensitive to the presence of surface contaminants such as water and hydrocarbons.[31] However, separate experiments of PAO6 on steel with a higher contact angle ($\theta_{sp} = 21°$) at 293 K[32] yields a very similar work of adhesion ($W_{sl} = 57$ mJ m^{-2}), which gives further confidence in our target value for the simulations. The higher work of adhesion at the steel/water interface than for steel/PAO4 suggests that the water nanofilm will be thermodynamically stable.[28] The discussion above indicates that the inability of previous force-fields to reproduce the work of adhesion of hematite/PAO4 interfaces[12] based on experimental contact angles[20] could be due to the absence of an interfacial water layer.

2. Experimental Section

There was no attempt to control the atmosphere in the contact angle experiments for PAO on steel[20,32] discussed above and the relative humidity was not reported. To cover the possible range of surface configurations in the experiments, we use fully hydroxylated surfaces[24] and water nanofilms with coverages ranging from 0 to 4 ML, which in the absence of a PAO4 layer corresponds to RH values of 5–95%.[24,25] Top-down views of the water films for the different water coverages (0.5–4 ML) are shown in **Figure 1a–e**. We show the interfacial structure of these nanoflims and demonstrate their important role in determining the work of adhesion in experimental systems, namely the hydroxylated α-Fe_2O_3(0001)/PAO4 interface.

Following our previous study,[12] PAO4 is represented by hydrogenated 1-decene trimer molecules, modeled with the LOPLS-AA force-field (FF)[34–36] and the internal surface interactions are from INTERFACE-FF.[18] The surfaces were generated using ASE[37] and had dimensions of 50 x 44 x 53 Å. We investigated the α-Fe_2O_3(0001) surface with a half-metal termination (R-Fe-O_3-Fe) and a hydroxylated oxygen termination (R-Fe-Fe-$(OH)_3$).[14] Since 1 ML coverages are reached at low RH (5%),[24] we only consider fully hydroxylated surfaces. The α-Fe_2O_3(0001) surfaces were fully hydroxylated by removing the terminal Fe layer and adding hydrogen atoms above the surface oxygens, yielding a hydroxyl coverage of 13.6 nm^{-2}.[25] Interactions in the solid hematite region were described by INTERFACE-FF[18] and the hydroxyl parameters were taken from ClayFF.[16] The SPC/E model[38] is used for the water molecules. Previous studies have confirmed that this model reproduces the experimental density dependence of the thermal conductivity of liquid water.[39] The 0.5, 1.0, 1.5, 3.0, and 4.0 ML water films contained 110, 220, 330, 660, and 880 water molecules each, respectively. The systems contained 220 PAO4 molecules on either side of the hematite surface. The systems had dimensions of 50 x 44 Å in x and y and a range of 237-259 Å in z, depending on water film thickness. Periodic boundary conditions were applied in all directions. For the solid-liquid interface, we compare three potentials with relatively weak (Clay-FF),[16,40] intermediate (INTERFACE-FF),[18] and strong (Savio et al.)[17] Lennard–Jones interactions. These span the possible interaction strengths that can be expected in experiments, with INTERFACE-FF[18] likely being the most accurate since wetting properties were included in the parameterization. The Lennard–Jones potential curves are shown for the Fe–C interactions for each force-field in the Supporting Information (Figure S1) and full parameters for each potential can be found in Table S1 (Supporting Information).

2.1. Work of Adhesion

Previous simulations have used the work of adhesion to parameterize interfacial force fields.[41] The work of adhesion has been shown to be correlated with the ITR in both experiments[42] and simulations.[43] Indeed, in our previous study with anhydrous surfaces,[12] we showed a clear correlation between the

© 2025 The Author(s). Advanced Materials Interfaces published by Wiley-VCH GmbH

21967350, 2025, 13, Downloaded from https://advanced.onlinelibrary.wiley.com/doi/10.1002/admi.202500267 by Imperial College London, Wiley Online Library on [06/10/2025]. See the Terms and Conditions (https://onlinelibrary.wiley.com/terms-and-conditions) on Wiley Online Library for rules of use; OA articles are governed by the applicable Creative Commons License

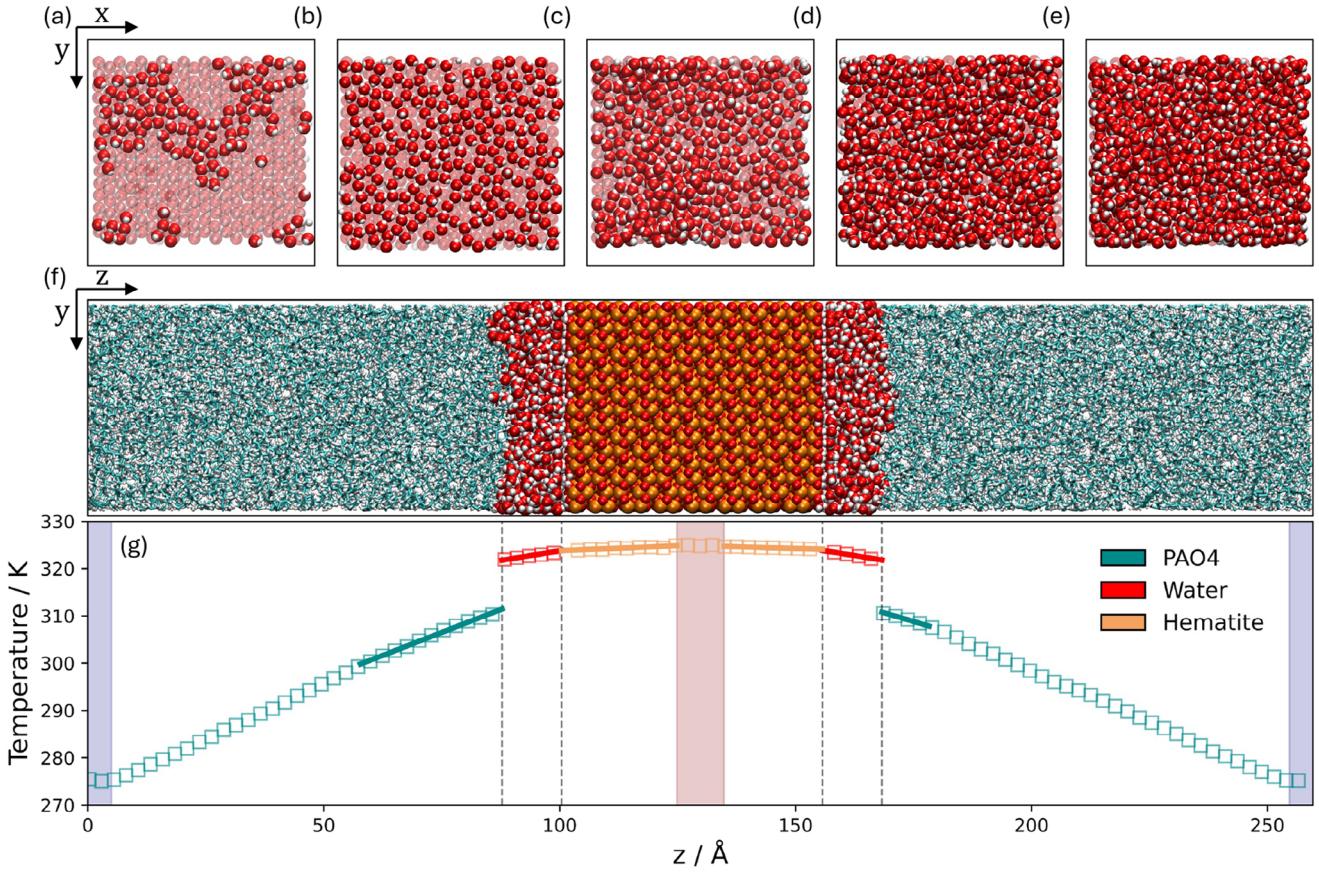


Figure 1. Top-down view of water films on fully hydroxylated hematite surface at varying coverages: a) 0.5 ML, b) 1.0 ML, c) 1.5 ML, d) 3.0 ML, and e) 4.0 ML. For clarity, only water and hydroxyl atoms are shown and the hydroxyl atoms are transparent. f) Side view of system used to calculate the ITR of the hydroxylated α-Fe_2O_3-water-PAO4 interface, shown for a water coverage of 4.0 ML and intermediate (INTERFACE-FF)[18] hematite-PAO4 interactions. Snapshots rendered using VMD.[33] Iron atoms are represented in orange, oxygen are red, carbon is cyan, and hydrogen is white. g) Through-film temperature profiles of the α-Fe_2O_3 surface (orange markers), water films (red markers) and PAO4 fluid (cyan markers). The red and blue shaded regions represent the positions of the hot and cold thermostats, respectively.

work of adhesion and the ITR. To quantify the surface wettability, we employ state-of-the-art computational methods based on the dry-surface approach.[19] An initial starting configuration for the work of adhesion calculations contained a 50 × 44 × 55 Å^3 hematite surface, with or without surface hydroxylation. The surface was placed between two liquid layers, first a water region with thicknesses 0-4 ML and then the PAO4 region, containing 220 molecules per side. The work of adhesion was calculated using the dry-surface method[19] with damped Coulomb interactions.[44] Using this method, hematite-PAO and water-PAO interactions were described by the potential:

$$U = \lambda[U_{LJ} + U_{Coul}] \tag{3}$$

where λ represents the coupling parameter. U_{LJ} was given by a Lennard Jones potential and U_{Coul} was given by a damped shifted force model, described by Fennel:[45]

$$U_{Coul} = q_i q_j \left[\frac{erfc(\alpha r)}{r} - \frac{erfc(\alpha r_c)}{r_c} + \left(\frac{erfc(\alpha r_c)}{r_c^2} + \frac{2\alpha}{\sqrt{\pi}} \frac{\exp(-\alpha^2 r_c^2)}{r_c} (r - r_c) \right) \right] \tag{4}$$

where q was the charge of particles i or j, $erfc()$ is the complementary error-function, α is the damping parameter and r_c is the cut-off distance of Coulombic interactions. The cutoff distance was set to a value of r_c = 12 Å and the damping parameter was set to a value of α = 0.2 Å^{-1}.

The simulation procedure was the same as used in our previous work.[12] All simulations were performed in LAMMPS[46] using velocity-Verlet integration with a timestep of 0.5 fs. The initial configurations were energy minimized, followed by a 1 ns equilibration in the NPT ensemble at 300 K with anisotropic pressure coupling set to 1 atm along the z-axis. A Nosé–Hoover thermostat and barostat[47–49] were employed, with temperature and pressure damping time constants of 0.1 ps and 1.0 ps, respectively. Subsequently, a 0.25 ns equilibration was performed in the NVT ensemble at 300 K using a Nosé-Hoover thermostat.[47,48] Production runs were performed in the NPT ensemble at T = 300 K and P = 1 atm in the z-direction using a Nosé-Hoover thermostat and barostat with damping coefficients of 0.1 ps and 1.0 ps, respectively.[47–49] LJ and Coulombic forces for hematite-PAO and water-PAO interactions were gradually switched off by scaling λ from λ = 1, which represents fully coupled surface-PAO4 interactions, to $\lambda \approx 0$, which represents fully uncoupled surface-PAO4

© 2025 The Author(s). Advanced Materials Interfaces published by Wiley-VCH GmbH

21967350, 2025, 13, Downloaded from https://advanced.onlinelibrary.wiley.com/doi/10.1002/admi.202500267 by Imperial College London, Wiley Online Library on [06/10/2025]. See the Terms and Conditions (https://onlinelibrary.wiley.com/terms-and-conditions) on Wiley Online Library for rules of use; OA articles are governed by the applicable Creative Commons License

interactions. The water monolayer was treated as part of the surface in these calculations, therefore, hematite-water interactions were maintained throughout the simulations.

λ, was sampled at 24 equally spaced data points in the range $\lambda \in (0,1]$. At each point, the system was equilibrated for 0.25 ns followed by a 0.75 ns run to obtain u_{sl}, the surface-liquid potential energy per unit area. The work of adhesion could be obtained using the equation:

$$W_{sl} = -\int_0^1 \left\langle \frac{\partial u_{sl}}{\partial \lambda} \right\rangle d\lambda \tag{5}$$

2.2. Interfacial Thermal Resistance

Previous NEMD simulations have shown that interfacial layers, such as graphene sheets[50] or surfactant monolayers adsorbed from solution,[51] can significantly affect the ITR at solid-liquid interfaces. Here we investigate the impact of water nanofilms by computing the ITR for the hydroxylated hematite/PAO4 interface using NEMD simulations.[52] Figure 1f shows a snapshot of a system with a water coverage of 4.0 ML used for both the ITR and the W_{sl} calculations, while an example temperature profile obtained from NEMD simulations is presented in Figure 1g. Simulations were performed using the same initial configurations as described above. However, in this case short range electrostatic forces were described using a Coulombic potential and long range electrostatic interactions were evaluated using the particle-particle particle-mesh (PPPM) solver[53] with a relative error in the forces of 1×10^{-5}.

The ITR was calculated using the boundary-driven NEMD approach[52] used in our previous work.[12] Five independent repeats were performed for each system, with each trajectory being given its own randomly generated initial velocity seed. The initial configurations were equilibrated following the same procedure described for the work of adhesion. To calculate the ITR, a heat flux was applied along the z-axis, by defining hot and cold thermostat regions in the xy plane, each with a thickness of 10 Å, located at the centre and the edge of the simulation box, respectively. The temperatures in these regions were maintained at 325 and 275 K for the hot and cold regions, respectively, using a Langevin thermostat.[54] A temperature damping coefficient of 1.0 ps was applied to ensure energy conservation during the NEMD simulations.[55] The NEMD simulations were performed for 5.5 ns, with the first 0.5 ns discarded to allow the system to reach a steady non-equilibrium state. Temperature profile were calculated by dividing the system into 400 bins along the z-axis and the temperature within each bin (b) was calculated using the equation:

$$T(b) = \frac{\sum_i^{N \in b} m_i v_i^2}{N_f k_B} \tag{6}$$

where m_i and v_i are the mass and velocities of a particle i within the bin and N_f is the total number of degrees of freedom in the bin. As the force fields used for hematite and PAO were fully flexible, $N_f = 3N_b$, where N_b was the number of atoms in each bin.[56] In the case of water, the local temperature needed to be corrected to account for the reduced degrees of freedom in rigid water model.[57] Oxygen and hydrogen temperature profiles were calculated separately where $N_f = 2.8106N_b$ for oxygen and $N_f = 1.5947N_b$ for hydrogen.[57]

2.3. MSD

The in-plane self-diffusion coefficient, D_{xy}, of the different water films, 0.5–4.0 ML, were calculated by analyzing the mean squared displacement (MSD) in the xy directions and applying the Einstein relation:

$$4D_{xy} = \frac{d\langle r_{xy}^2(t)\rangle}{dt} \tag{7}$$

where $\langle r_{xy}^2(t)\rangle$ is the MSD in the xy plane at time, t, given by:

$$\langle r_{xy}^2(t)\rangle = \langle r_x^2(t)\rangle + \langle r_y^2(t)\rangle \tag{8}$$

The MSD components in the x and y directions are computed as:

$$\langle r_x^2(t)\rangle = \frac{1}{N}\sum_{i=1}^{N}(x_i(t) - x_i(0))^2 \tag{9}$$

$$\langle r_y^2(t)\rangle = \frac{1}{N}\sum_{i=1}^{N}(y_i(t) - y_i(0))^2 \tag{10}$$

where N is the total number of molecules, $x(t)$ and $y(t)$ are the coordinates of molecule i at time t, and $x(0)$ and $y(0)$ are the initial coordinates at $t = 0$.

3. Results and Discussion

Figure 2 shows the mass density and temperature profiles for the systems considered in this study. Results are shown only for INTERFACE-FF,[18] the equivalent plots for ClayFF[16] and the Savio et al.[17] force field are shown in the Supporting Information (Figure S2 and Figure S3, respectively). The apparent non-linearity and fluctuations observed in the temperature profiles within the hematite slab are due to statistical noise in bins containing relatively few atoms. Surface hydroxylation has previously been shown to increase the hydrophilicity of hematite[23] and other oxides, such as silica,[58] due to increased hydrogen bonding. This hydrophilicity is confirmed by a pronounced peak in the water mass density profile close to the hydroxylated hematite/water interface in Figure 2b–f. This sharp peak near the surface indicates a dense layering of water molecules, which is known to enhance thermal conductivity and reduce the ITR.[59,60] As a result, we observe a very small temperature drop at the hydroxylated hematite/water interface and therefore an almost negligible ITR of ~ 0.3 K m^2 GW^{-1}. Throughout the simulations, the water molecules remained close to the hydroxylated surface due to strong hydrogen bonding interactions and their low solubility in PAO4, which naturally prevented diffusion into the oil.

The behaviour of the PAO4 fluid also varies with water coverage. For the anhydrous (not pictured) and the hydroxylated system (Figure 2a), strong layering is observed in the PAO4 density

© 2025 The Author(s). Advanced Materials Interfaces published by Wiley-VCH GmbH

21967350, 2025, 13, Downloaded from https://advanced.onlinelibrary.wiley.com/doi/10.1002/admi.202500267 by Imperial College London, Wiley Online Library on [06/10/2025]. See the Terms and Conditions (https://onlinelibrary.wiley.com/terms-and-conditions) on Wiley Online Library for rules of use; OA articles are governed by the applicable Creative Commons License

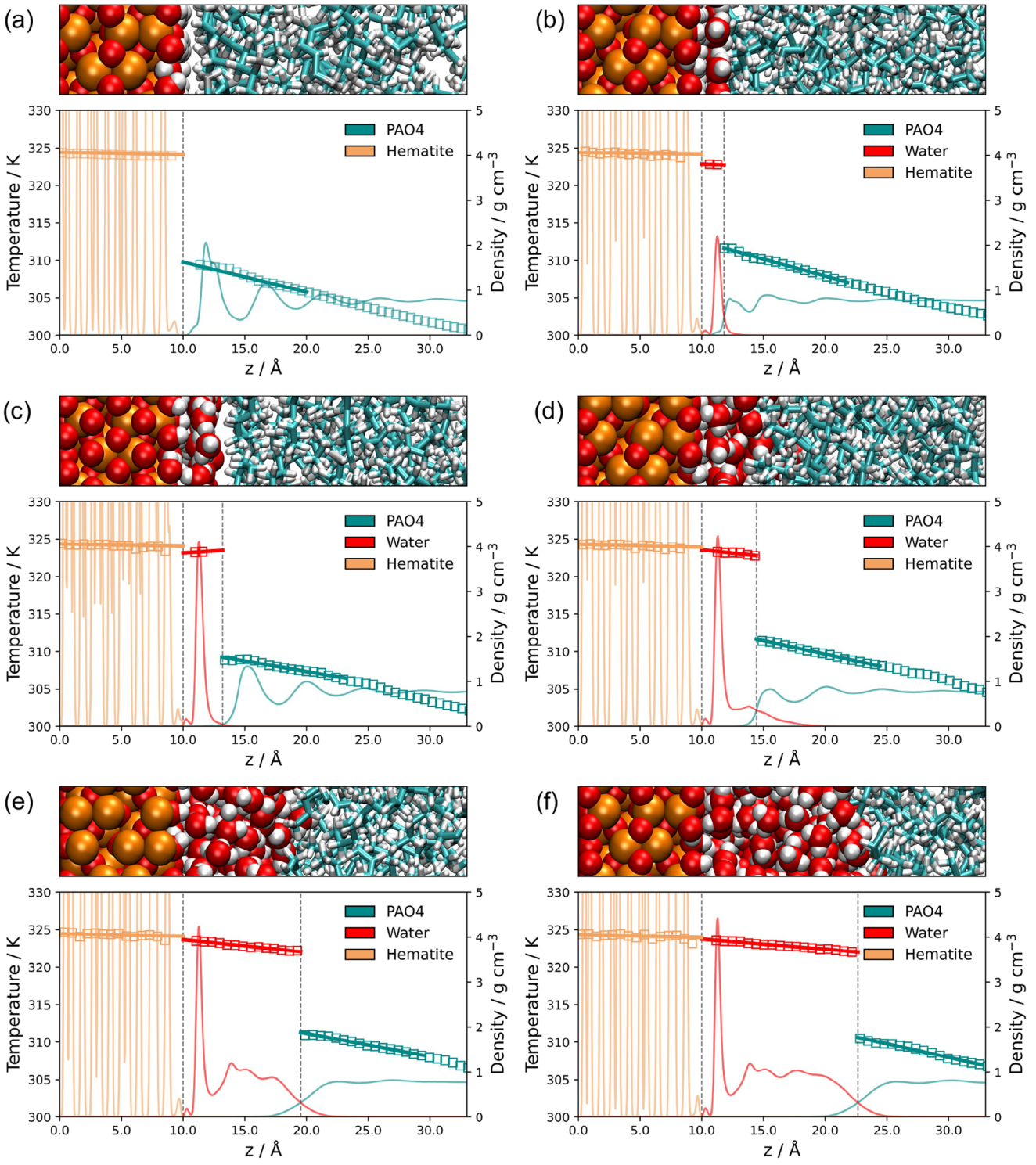


Figure 2. Temperature (symbols) and density (lines) profiles for the hydroxylated surfaces with a) 0, b) 0.5, c) 1.0, d) 1.5, e) 3.0, and f) 4.0 ML water coverage. Results shown for the intermediate (INTERFACE-FF)[18] interactions. The vertical dashed lines represent the interfaces between the surface, water and PAO4 regions. The thick solid lines represent the linear fit temperature profiles within these regions. Data points outside of the fitting regions and in regions of low density have been removed for clarity. Zoomed-in snapshots of the systems rendered using VMD.[33]

© 2025 The Author(s). Advanced Materials Interfaces published by Wiley-VCH GmbH

21967350, 2025, 13, Downloaded from https://advanced.onlinelibrary.wiley.com/doi/10.1002/admi.202500267 by Imperial College London, Wiley Online Library on [06/10/2025]. See the Terms and Conditions (https://onlinelibrary.wiley.com/terms-and-conditions) on Wiley Online Library for rules of use; OA articles are governed by the applicable Creative Commons License

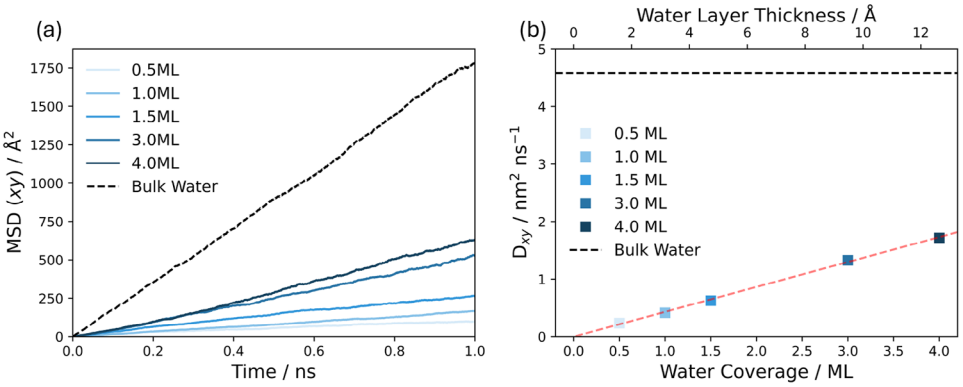


Figure 3. a) Mean squared displacement (MSD) in the *xy* plane for water molecules in water films of varying coverages and bulk water. b) In-plane self-diffusion coefficient (D_{xy}) plotted as a function of water coverage (lower axis) and water layer thickness (upper axis), calculated at 325 K. The dashed horizontal line represents the results calculated from bulk water simulations at 325 K. Note that the data is plotted for water coverage, and while the water layer thickness values do not exactly align, they are included as an approximate guide.

profile, with a pronounced first density peak that is strongly dependent on the strength of the solid-liquid interactions.[12] However, as the thickness of the water film increases the PAO4 structure becomes progressively less ordered. By 3.0 and 4.0 ML coverage, the first PAO4 density peak is substantially reduced, and density oscillations in the PAO4 layer are no longer apparent. This may be due to the screening of the hematite-PAO4 interactions by the hydroxyl groups and water molecules. However, thermal capillary wave (CW) fluctuations, which are reduced when the water film is in contact with the solid surface, may also play a role. These fluctuations smooth out the apparent layering of water and PAO4 molecules, especially for thick water films, even though the underlying structure remains intact.[61]

For the 0.5 ML water system (Figure 2b), both water and PAO4 molecules are in direct contact with the hydroxylated hematite surface, as evidenced by the overlapping first density peak and the inhomogeneous density profile, indicating a mixed interface for thermal transport. At 1 ML water coverage (Figure 2c), the density profiles show limited direct contact between the PAO4 molecules and the surface, with the in-plane density profile revealing a homogeneous interface. For water coverages above 1 ML (Figure 2d–f), there is an apparent overlap in the density profiles for the water and PAO4 molecules, suggesting an interface width of ~5 Å. However, this may also result from CW fluctuations, which blur the sharpness of the interfacial structure despite the presence of molecular layering.[61]

To determine the mobility of the confined water molecules, we tracked the mean square displacement, for all water molecules contrained in the film, in the surface plane to calculate the self-diffusion coefficient at 325 K, D_{xy}, as shown in **Figure 3**. D_{xy} decreases significantly from 4 ML (1.72 $nm^2\ ns^{-1}$) to 0.5 ML (0.23 $nm^2\ ns^{-1}$), where a higher proportion of the water molecules are immobilized close to the surface. This observation is consistent with previous MD simulations of hydrophilic surfaces.[62] In contrast, the self-diffusion coefficient for bulk water at 325 K was 4.58 $nm^2\ ns^{-1}$, which is close to the experimental value at this temperature, $D = 4.1\ nm^2\ ns^{-1}$.[63] Despite their reduced mobility near the surface, the water molecules remain diffusive, suggesting that they do not solidify as has been observed for some other surfaces such as mica.[64] This is further confirmed by the oxygen-oxygen radial distribution functions (RDFs) shown in the Supporting Information (Figure S4), which do not exhibit any long-range order. Unlike some other minerals, ice nucleation does not occur for the α-Fe_2O_3(0001) surface due to the large mismatch with the basal plane triangular lattice.[65]

The work of adhesion at 300 K is presented in **Figure 4** as a function of water coverage for weak (ClayFF),[16] intermediate (INTERFACE-FF),[18] and strong (Savio et al.)[17] solid-liquid interactions. In our previous study, we observed that for anhydrous α-Fe_2O_3(0001) surfaces, W_{sl} was strongly dependent on solid–liquid interaction strength, with W_{sl} being overestimated in all cases.[12] For hydroxylated surfaces without water (filled markers, 0 ML), W_{sl} was reduced with respect to the non-hydroxylated anhydrous surfaces (unfilled markers, 0 ML) for all three FFs. W_{sl} was still overestimated compared to the experimental value,[20] apart from the low interaction strength FF (ClayFF),[16] where

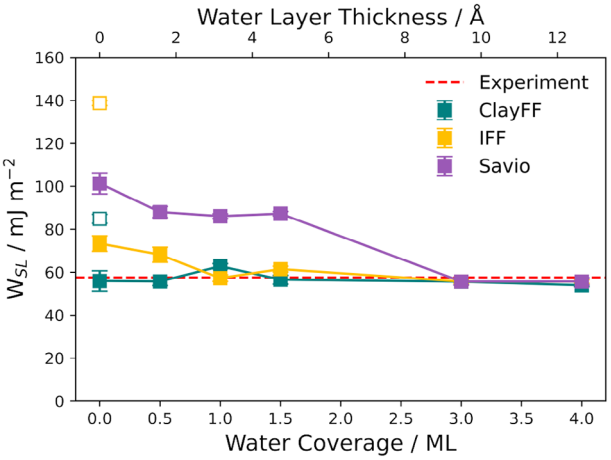


Figure 4. Work of adhesion, W_{sl}, as a function of water coverage for the low (ClayFF),[16] intermediate (INTERFACE-FF),[18] and high (Savio et al.)[17] solid-liquid interaction strengths. Anhydrous and hydroxylated surfaces are represented by unfilled and filled markers, respectively. The result for the anhydrous surface with the Savio et al. force field ($W_{sl} = 405\ mJ\ m^{-2}$) is not shown. Experimental W_{sl} is calculated from the contact angle of PAO4 on steel reported by Kalin and Polajnar.[20]

© 2025 The Author(s). Advanced Materials Interfaces published by Wiley-VCH GmbH

21967350, 2025, 13, Downloaded from https://advanced.onlinelibrary.wiley.com/doi/10.1002/admi.202500267 by Imperial College London, Wiley Online Library on [06/10/2025]. See the Terms and Conditions (https://onlinelibrary.wiley.com/terms-and-conditions) on Wiley Online Library for rules of use; OA articles are governed by the applicable Creative Commons License

surface hydroxylation alone led to good agreement. For the other two FFs (INTERFACE-FF[18] and Savio et al.),[17] the inclusion of a partial water monolayer (0.5 ML) led to a further reduction in W_{sl}; however, we still observed a considerable overestimation in W_{sl}. Increasing the water film thickness led to further reductions in W_{sl} for the intermediate and strong interaction FFs, while W_{sl} for the weak interactions remained consistent with the experimental value. For intermediate interactions, W_{sl} aligned with the experimental value at water coverages $\geqslant$ 1.0 ML, whereas for strong interactions, agreement was only achieved at a film thickness of $\geqslant$ 3.0 ML. When the water layer is included, the hematite/PAO4 interactions are screened, and the work of adhesion eventually becomes dominated by the water/PAO4 interactions. The stronger the hematite/PAO4 interactions, the thicker the water film required to fully screen them. Once these interactions are fully screened, W_{sl} becomes independent of the water coverage and consistently matches the experimental value.[20] The result at 4.0 ML effectively represents W_{sl} for the water/PAO4 interface, as the PAO4 is decoupled from hematite surface due to the thickness of the water film. This result is in reasonable agreement with the expected value from the work of Aveyard and Haydon (W_{sl} = 52 mJ m^{-2}), based on the number of methylene and methyl groups in the PAO4 molecules.[66]

To quantify the ITR of the hematite/water/PAO4 interface, we considered the overall ITR, R_{Total}, using a thermal circuit in series:

$$R_{total} = R_{hem/water} + R_{water} + R_{water/PAO} \tag{11}$$

where $R_{hem/water}$ the ITR of the hematite/water interface, R_{water} is the thermal resistance per unit area of the water film and $R_{water/PAO}$ is the ITR of the water/PAO4 interface. R_{water} was calculated according to:

$$R_{water} = \frac{L}{\kappa_{water}} \tag{12}$$

where L and κ_{water} are the thickness and the thermal conductivity of the water film, respectively. κ_{water} was calculated using Fourier's law:[67]

$$\lambda = -\frac{J_q}{\nabla T} \tag{13}$$

where ∇T is the temperature gradient obtained from the water temperature profiles.

The total ITR for the different FFs and water coverages is shown in **Figure 5**a, and the contributions of each component are shown for each forcefield in Figure 5b–d. For the 0.5 and 1.0 ML films, the R_{water} was assumed to be negligible as the films were $\leqslant$ 1 molecule thick. However, as the water coverage increases, this contribution becomes more significant. Even for the thickest water films, R_{water} is much smaller than $R_{water/PAO}$, which is due to the relatively high thermal conductivity of water compared to PAO.[3]

The magnitude of the interfacial potential energy is presented as a function of water film thickness for the 3 force-fields in the Supporting Information (Figure S5). This was calculated by summing all of the pairwise energies (LJ and Coulombic) between the surface atoms (Hematite and water film) and the PAO4 atoms. As the film thickness increases, the interfacial potential energy decreases and converges towards a consistent value of ~ 300 kcal/mol due to the screening of the Hematite/PAO4 interactions by the water film. At water coverages of > 0.5 ML, the water layer entirely screens the low (ClayFF)[16] and intermediate (INTERFACE-FF)[18] hematite-PAO4 interactions, which means that the ITR is mainly dependent on the water/hematite and water/PAO4 interactions. Since water/hematite and water/PAO4 interactions remain constant, we see a similar ITR for the weak and intermediate interactions for water coverages of 0.5 ML and above. In the case with high solid-liquid interaction strengths (Savio et al.),[17] the hematite/PAO4 interactions are strong enough to be felt by the PAO4 molecules in the presence of thicker water films; however, the increased water film thickness leads to an increased screening of these interactions and therefore an increase in ITR. For thinner films, the ITR at the water/PAO4 interface is controlled by both the water/PAO4 interactions and the hematite/PAO4 interactions, leading to a lower ITR. At 1.5 ML coverage and above, the hematite/PAO4 interactions are almost entirely screened by the water layer and the ITR converges with the weak and intermediate FFs. The water layer isolates the PAO4 from the surface and the ITR at the water/PAO4 interface is governed only by the water/PAO4 interactions. Unlike for the anhydrous hematite/PAO4 interface,[12] there is no clear correlation between R_k and W_{sl}, as shown in the Supporting Information (Figure S6). This has also been noted from previous NEMD simulations of the interface between a hydroxylated surface and hydrocarbons.[68] This observation is likely due to the screening effects of the hydroxyls and water molecules.

The ITR at the hydroxylated hematite/water interface was found to be very low (~ 0.3 m^2 K GW^{-1}). This can be attributed to strong interfacial hydrogen bonding, which enhances vibrational coupling across the interface and promotes more efficient energy transfer compared to van der Waals-dominated interactions at the hematite/PAO and water/PAO interfaces.[69] To demonstrate this, we analyzed the vibrational density of states (VDOS) for water and PAO4 molecules near the surface (Figure S7, Supporting Information). The VDOS was obtained from the Fourier transform of the velocity autocorrelation function (VACF), with a correlation time of 4 ps:

$$D_\alpha(\omega) = \int_0^\infty \langle \mathbf{v}_\alpha(0)\mathbf{v}_\alpha(t)\rangle \cdot e^{-2\pi i\omega t}\, dt \tag{14}$$

where $\langle \mathbf{v}_\alpha(0)\mathbf{v}_\alpha(t)\rangle$ is the VACF of species α, and ω is the frequency. To capture the behaviour of the interfacial atoms, the VDOS was computed for atoms within a 2 Å region on either side of the interface.

To quantify the degree of overlap in the VDOS, the overlap integral, S, was calculated according to the equation:[70,71]

$$S = \frac{\int_0^\infty D_{fluid}(\omega) D_{\text{surface}}(\omega) d\omega}{\int_0^\infty D_{fluid}(\omega) d\omega \int_0^\infty D_{\text{surface}}(\omega) d\omega} \tag{15}$$

where D_{fluid} is the VDOS for the PAO or water regions close to the hematite surface and D_{surface} is the VDOS for the surface. The overlap integral for the hydroxyl/ water interface (S = 4.1×10^{-3}) is almost double that of the overlap integral for the

© 2025 The Author(s). Advanced Materials Interfaces published by Wiley-VCH GmbH

21967350, 2025, 13, Downloaded from https://advanced.onlinelibrary.wiley.com/doi/10.1002/admi.202500267 by Imperial College London, Wiley Online Library on [06/10/2025]. See the Terms and Conditions (https://onlinelibrary.wiley.com/terms-and-conditions) on Wiley Online Library for rules of use; OA articles are governed by the applicable Creative Commons License

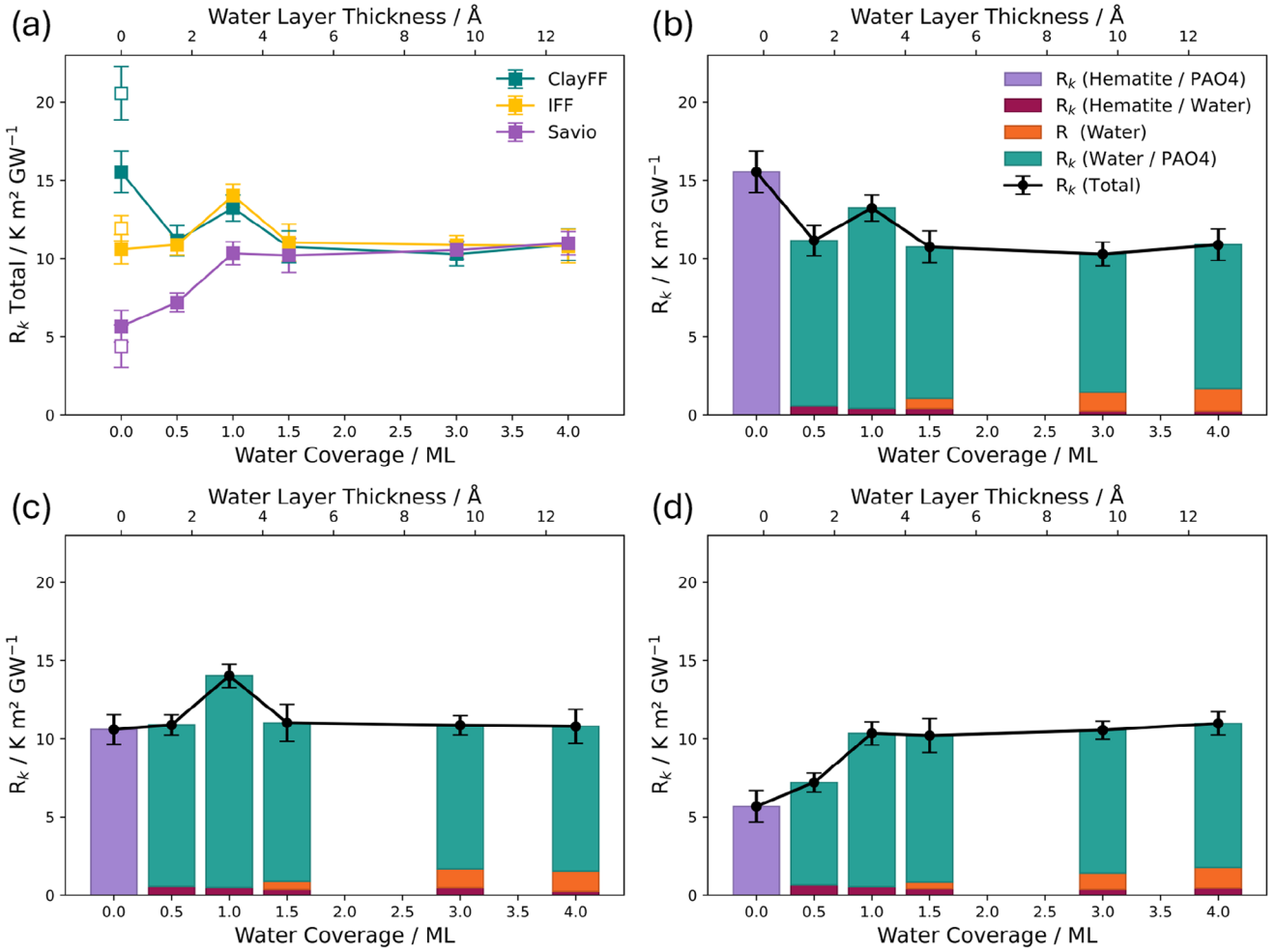


Figure 5. a) Interfacial thermal resistance, R_k, shown as a function of water-coverage. Results are displayed for low (ClayFF),[16] intermediate (INTERFACE-FF),[18] and high (Savio et al.)[17] solid–liquid interaction strengths. Anhydrous and hydroxylated surfaces are represented by unfilled and filled symbols, respectively. b–d) Total ITR and its contributions to the hematite/water/PAO4 ITR are shown for weak (ClayFF)[16] (b), intermediate (INTERFACE-FF)[18] (c), and strong (Savio et al.)[17] (d) solid-liquid interactions. The bar plots show the total ITR (solid black line) and its contributions: hematite/water ITR (maroon), water thermal resistance (orange), water/PAO ITR (teal) and hematite/PAO4 ITR (purple). Anhydrous surface results are not displayed.

hydroxyl/PAO4 interface ($S = 2.5 \times 10^{-3}$), partially explaining the lower ITR at this interface.

Our calculated ITR for the hematite/water interface (~ 0.3 m^2 K GW^{-1}) was somewhat lower than the value reported by Gonzalez-Valle et al.[69] for water-alumina interfaces (~ 4.5 m^2 K GW^{-1}). This discrepancy may arise from differences in both charge equilibration methods and the nature of the surfaces studied. Their work employed reactive MD simulations to dynamically adjust partial charges, mitigating the overestimation of Coulombic interactions. In contrast, our simulations did not include this correction, potentially leading to stronger Coulombic interactions and artificially enhanced interfacial bonding, which would lower the ITR. Additionally, hematite and alumina have distinct surface chemistries which could further influence interfacial bonding and energy transfer.

The contribution of the thermal resistance of the water film, which increased with the thickness of the film, was generally not a major contributor to the total ITR, as shown in Figure 5b–d. Instead, the total ITR is dominated by the liquid-liquid (PAO/water) interface. Water and alkanes such as PAO4 exhibit low solubility, which is known to lead to a large ITR.[72]

The water/PAO4 ITR was found to be dependent on the structure of the water film near the interface. The water/PAO4 ITR is presented as a function of the water film thickness, for each forcefield, in the Supporting Information (Figure S8). For 0.5 ML water coverage, the incomplete surface coverage results in a heterogeneous interface with overlapping density profiles of PAO4 and water (Figure 2b). This resulted in a lower ITR with respect to films with 1.0 ML coverage, where the water forms a densely packed and highly structured layer with negligible overlap observed in the density profiles (Figure 2c).

For the low (ClayFF)[16] and intermediate (INTERFACE-FF)[18] hematite-PAO4 interactions, a noticeable spike in the total ITR is observed for the 1.0 ML water films. To better understand this observation, we calculated the surface area of the water/PAO4 interface by generating a height map from the atomic positions of

© 2025 The Author(s). Advanced Materials Interfaces published by Wiley-VCH GmbH

21967350, 2025, 13, Downloaded from https://advanced.onlinelibrary.wiley.com/doi/10.1002/admi.202500267 by Imperial College London, Wiley Online Library on [06/10/2025]. See the Terms and Conditions (https://onlinelibrary.wiley.com/terms-and-conditions) on Wiley Online Library for rules of use; OA articles are governed by the applicable Creative Commons License

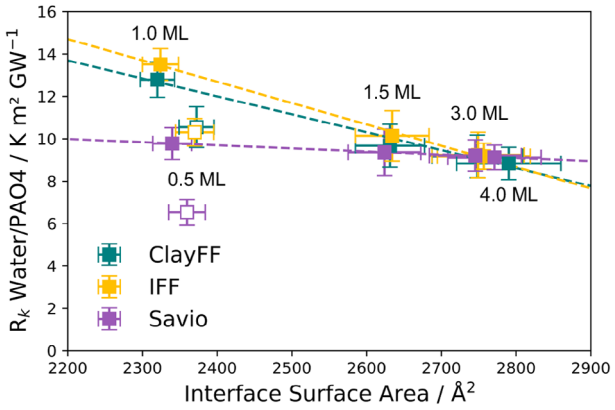


Figure 6. Interfacial thermal resistance, R_k, shown as a function of the water/PAO4 interface surface area for the low (ClayFF),[16] intermediate (INTERFACE-FF),[18] and high (Savio et al.)[17] solid-liquid interaction strengths at different water coverages. Results for the 0.5 ML water films are represented by unfilled markers and are not included in linear fits.

the water film. The areas of the resulting quadrilateral elements were then summed. Height maps for different water films are provided in the Supporting Information (Figure S9).

The water/PAO4 ITR is plotted as a function of the interface surface area in **Figure 6** for different water coverages. The 0.5 ML results are shown as unfilled markers because the water layer does not cover the surface and some PAO molecules are in direct contact with the surface. For low (ClayFF)[16] and intermediate (INTERFACE-FF)[18] hematite-PAO4 interactions, the ITR decreases with increasing surface area. This is consistent with a previous MD study, where it was noted that an increased effective contact area between a self-assembled monolayer and an organic liquid enhanced interfacial thermal transport.[73] Furthermore, Shavelier et al.[74] observed that interfacial thermal conductance was higher in systems where there was greater physical overlap between ligands and solvent molecules for gold surfaces and nanoparticles functionalized with MTAB (16-mercaptohexadecyl-trimethylammonium bromide) compared to CTAB (cetyltrimethylammonium bromide).

For the high hematite-PAO4 interaction strength (Savio et al.),[17] the ITR is less sensitive to the surface area. This can be explained by the competing effect of the interfacial potential energy[73] as the water coverage increases. For the low (ClayFF)[16] and intermediate (INTERFACE-FF)[18] hematite-PAO4 interactions, the interfacial potential remains roughly constant across different water coverages, as shown in the Supporting Information (Figure S5). This is due to screening effects, meaning that the PAO/water surface area is the dominant factor in determining ITR. For strong hematite-PAO4 interactions (Savio et al.),[17] increasing the water coverage results in a significant reduction in the interfacial potential. This reduction in interfacial potential increases the ITR,[73] counteracting the decrease in ITR caused by the increase in surface area for higher water coverage. Furthermore, analysis of the vibrational density of states (VDOS) showed that the vibrational mismatch between the water and the PAO was the same for all systems, and as such, the changes in ITR can be attributed to the surface area contact and the interfacial potential energy. VDOS for different water are displayed in the Supporting Information (Figure S10).

4. Conclusion

In our previous study,[12] we observed a wide range of ITR values for the anhydrous α-Fe_2O_3(0001)/PAO4 interface (R_k = 4-21 K m^2 GW^{-1}) depending on the strength of the solid-liquid interaction potential. To match the work of adhesion calculated from contact angle experiments at the steel/PAO4 interface,[20] we had to further reduce the strength of the weakest solid-liquid interaction potential, which led to a large ITR of 33 m^2 K GW^{-1}.[12] Here, we match the experimental work of adhesion by incorporating surface hydroxylation and water nanolayers of varying thickness at the hematite/PAO4 interface. For the weak (ClayFF)[16] interaction potential, the simulated work of adhesion aligned with the experimental value with full surface hydroxylation and across all tested water film thicknesses (0–4 ML). For intermediate (INTERFACE-FF)[18] solid-liquid interactions, good agreement with the experimental work of adhesion occurred with hydroxylated surfaces featuring water films $\geqslant$ 1.0 ML, while for strong (Savio et al.)[17] interactions, the match was observed with water films $\geqslant$ 3.0 ML. Previous experiments have suggested that water coverages of $\geqslant$ 3.0 ML only form at very high relative humidities (>85%),[25] while water films < 1.0 ML require low relative humidities (<10%).[24] Although the relative humidity conditions for the experiments used to calculate the work of adhesion are unspecified,[20] it is likely that the steel surface in the experiments had a water film in the 1.0–1.5 ML range.[24] Thus, the strong (Savio et al.)[17] interaction potential overestimates the adhesive forces between hematite and PAO. Therefore, we suggest that future NEMD simulations use the weak (ClayFF)[16] or intermediate (INTERFACE-FF)[18] potentials with 1.0–1.5 ML of water coverage for a more accurate representation of the experimental interface.

Surface hydroxylation and the inclusion of interfacial water nanofilms also significantly impact the ITR. For water films thicker than one monolayer, the ITR converges to a consistent value ($R_k \approx$ 10 m^2 K GW^{-1}) that is independent of the solid–liquid interaction strength. This corresponds to a thermal slip length or Kapitza length of 1.4 nm.[75] This value is primarily governed by the ITR at the water/PAO interface, with strong hydrogen bonding between the water film and the hydroxylated surface resulting in a very small hematite/water ITR. Previous NEMD simulations reported a similar ITR at the water/octane (R_k = 15 m^2 K GW^{-1}) and water/benzene (R_k = 6 m^2 K GW^{-1}) interfaces, with the latter having stronger intermolecular interactions and increased first layer density.[76] Thus, our value of the ITR sits between those previously measured for water/hydrocarbon interfaces. Notably, we observed that the structure of the water film directly influenced the interfacial surface area, which in turn impacted the water/PAO ITR. For thinner water films, particularly at 1.0 ML, the interface exhibited minimal roughness, leading to a lower effective surface area and an increased ITR. As film thickness increased, interfacial roughness and surface area grew, reducing the ITR due to improved thermal contact. By incorporating surface hydration, closely reflecting the nanoscale surface structure expected in experiments under ambient conditions, these simulations offer a more precise estimate of the

© 2025 The Author(s). Advanced Materials Interfaces published by Wiley-VCH GmbH

21967350, 2025, 13, Downloaded from https://advanced.onlinelibrary.wiley.com/doi/10.1002/admi.202500267 by Imperial College London, Wiley Online Library on [06/10/2025]. See the Terms and Conditions (https://onlinelibrary.wiley.com/terms-and-conditions) on Wiley Online Library for rules of use; OA articles are governed by the applicable Creative Commons License

ITR at the hematite/PAO interface. This ITR value should prove useful for thermal modeling of systems such as oil-based iron oxide nanofluids, and nanoscale thermal management systems such as nano-engineered surfaces.[77–79] We also hope that the ITR value from our simulations will be experimentally validated for the hematite/PAO interface using thermoreflectance-based techniques[7] in the near future.

We suggest that water nanolayers should also be accounted for in future MD simulations of hematite/hydrocarbon interfaces to study adsorption,[80] friction[81] and velocity slip.[17] While some previous studies have included iron oxide surfaces with hydroxylation[82] or water nanofilms,[83,84] the vast majority have used anhydrous surfaces. One caveat to this recommendation is for high-temperature applications of hematite/hydrocarbon interfaces, since previous experiments suggest that surface hydrophobicity is restored above 60 °C.[23] One application where anhydrous surfaces may be more appropriate is engine lubricants, as their operational temperature often exceeds 100 °C,[85] so any surface-bound water and hydroxylation is likely to be removed.[23] We also expect our nanoscale insights to be relevant to the interfaces between hydrocarbons and other oxide surfaces (e.g., silica,[26] alumina,[26] quartz,[27] sapphire,[27] and mica)[28] where water nanofilms are also known to form.

Supporting Information

Supporting Information is available from the Wiley Online Library or from the author.

Acknowledgements

F.C., D.D., and J.P.E. contributed equally to this work. F.C. thanks the UK Department of Science, Innovation and Technology (DSIT), the Engineering and Physical Sciences Research Council (EPSRC), and Shell for PhD funding through the InFUSE Prosperity Partnership (EP/V038044/1). J.P.E. was supported by DSIT and the Royal Academy of Engineering (RAEng) through the Research Fellowships scheme. D.D. was supported by DSIT, RAEng, and Shell via a Research Chair in Complex Engineering Interfaces. F.B. thanks the Leverhulme Trust for funding. The authors acknowledge the use of Imperial College London Research Computing Service (https://doi.org/10.14469/hpc/2232) and the UK Materials and Molecular Modelling Hub, which is partially funded by the EPSRC (EP/T022213/1, EP/W032260/1 and EP/P020194/1). The authors thank Carlos Corral-Casas for useful discussions.

Conflict of Interest

The authors declare no conflict of interest.

Data Availability Statement

The data that support the findings of this study are available from the corresponding author upon reasonable request.

Keywords

interfacial thermal resistance, molecular dynamics simulations, work of adhesion

Received: April 4, 2025
Revised: May 14, 2025
Published online: June 17, 2025

[1] B. V. Grinsven, K. Eersels, M. Peeters, P. Losada-Pérez, T. Vandenryt, T. J. Cleij, P. Wagner, *ACS Appl. Mater. Interfaces* **2014**, *6*, 13309.
[2] J. P. Ewen, H. Gao, M. H. Müser, D. Dini, *Phys. Chem. Chem. Phys.* **2019**, *21*, 5813.
[3] E. Harika, J. Bouyer, M. Fillon, M. Helene, *J. Tribol.* **2013**, *135*, 041707.
[4] Y. Deng, C. Feng, J. E, H. Zhu, J. Chen, M. Wen, H. Yin, *Appl. Therm. Eng.* **2018**, *142*, 10.
[5] X. Wang, B. Li, D. Gerada, K. Huang, I. Stone, S. Worrall, Y. Yan, *Appl. Therm. Eng.* **2022**, *201*, 117758.
[6] S. M. S. Murshed, C. A. N. de Castro, *Renew. Sustain.Energy Rev.* **2017**, *78*, 821.
[7] J. Chen, X. Xu, J. Zhou, B. Li, *Rev. Mod. Phys.* **2022**, *94*, 025002.
[8] P. Zhang, P. Yuan, X. Jiang, S. Zhai, J. Zeng, Y. Xian, H. Qin, D. Yang, *Small* **2018**, *14*, 1702769.
[9] K. S. Suganthi, K. S. Rajan, *Renew. Sustain.Energy Rev.* **2017**, *76*, 226.
[10] C. Roe, X. Feng, G. White, R. Li, H. Wang, X. Rui, C. Li, F. Zhang, V. Null, M. Parkes, Y. Patel, Y. Wang, H. Wang, M. Ouyang, G. Offer, B. Wu, *J. Power Sources* **2022**, *525*, 231094.
[11] H. Berro, N. Fillot, P. Vergne, *Tribol. Int.* **2010**, *43*, 1811.
[12] F. Carman, J. P. Ewen, F. Bresme, B. Wu, D. Dini, *ACS Appl. Mater. Interfaces* **2024**, *16*, 59452.
[13] R. Y. Chen, W. Y. Yuen, *Oxid. Met.* **2003**, *59*, 433.
[14] G. S. Parkinson, *Surf. Sci. Rep.* **2016**, *71*, 272.
[15] P. D. Shima, J. Philip, B. Raj, *J. Phys. Chem. C* **2010**, *114*, 18825.
[16] R. T. Cygan, J.-J. Liang, A. G. Kalinichev, *J. Phys. Chem. B* **2004**, *108*, 1255.
[17] D. Savio, N. Fillot, P. Vergne, M. Zaccheddu, *Tribol. Lett.* **2012**, *46*, 11.
[18] K. Kanhaiya, M. Nathanson, P. J. in 't Veld, C. Zhu, I. Nikiforov, E. B. Tadmor, Y. K. Choi, W. Im, R. K. Mishra, H. Heinz, *J. Chem. Theory Comput.* **2023**, *19*, 8293.
[19] F. Leroy, F. Müller-Plathe, *Langmuir* **2015**, *31*, 8335.
[20] M. Kalin, M. Polajnar, *Appl. Surf. Sci.* **2014**, *293*, 97.
[21] F. Sun, T. Zhang, M. M. Jobbins, Z. Guo, X. Zhang, Z. Zheng, D. Tang, S. Ptasinska, T. Luo, *Adv. Mater.* **2014**, *26*, 6093.
[22] M. Sterrer, N. Nilius, S. Shaikhutdinov, M. Heyde, T. Schmidt, H.-J. Freund, *J. Mater. Res.* **2019**, *34*, 360.
[23] K. Shrimali, J. Jin, B. V. Hassas, X. Wang, J. D. Miller, *J. Colloid Interface Sci.* **2016**, *477*, 16.
[24] S. Yamamoto, T. Kendelewicz, J. T. Newberg, G. Ketteler, D. E. Starr, E. R. Mysak, K. J. Andersson, H. Ogasawara, H. Bluhm, M. Salmeron, G. E. Brown, A. Nilsson, *J. Phys. Chem. C* **2010**, *114*, 2256.
[25] J.-F. Boily, M. Yeşilbaş, M. Md. Musleh Uddin, L. Baiqing, Y. Trushkina, G. Salazar-Alvarez, *Langmuir* **2015**, *31*, 13127.
[26] H. W. Fox, E. F. Hare, W. A. Zisman, *J. Phys. Chem.* **1955**, *59*, 1067.
[27] M. K. Bernett, W. A. Zisman, *J. Colloid Interface Sci.* **1969**, *29*, 413.
[28] C. Cafolla, K. Voïtchovsky, *Nanoscale* **2020**, *12*, 14504.
[29] Z. Yang, N. L. Abbott, *Langmuir* **2010**, *26*, 13797.
[30] J. H. Clint, *Curr. Opin. Colloid Interface Sci.* **2001**, *6*, 28.
[31] R. A. Gledhill, A. J. Kinloch, S. J. Shaw, *J. Adhes.* **1977**, *9*, 81.
[32] M. A. C. de Sousa Marques, M. J. Guimarey, V. Domínguez-Arca, A. Amigo, J. Fernández, *Thermochim. Acta* **2021**, *703*, 178994.
[33] W. Humphrey, A. Dalke, K. Schulten, *J. Mol. Graphics* **1996**, *14*, 33.
[34] W. L. Jorgensen, D. S. Maxwell, J. Tirado-Rives, *J. Am. Chem. Soc.* **1996**, *118*, 11225.
[35] M. L. P. Price, D. Ostrovsky, W. L. Jorgensen, *J. Comput. Chem.* **2001**, *22*, 1340.
[36] S. W. I. Siu, K. Pluhackova, R. A. Böckmann, *J. Chem. Theory Comput.* **2012**, *8*, 1459.
[37] A. H. Larsen, J. J. Mortensen, J. Blomqvist, I. E. Castelli, R. Christensen, M. Dułak, J. Friis, M. N. Groves, B. Hammer, C. Hargus, E. D. Hermes, P. C. Jennings, P. B. Jensen, J. Kermode, J. R. Kitchin, E. L. Kolsbjerg, J. Kubal, K. Kaasbjerg, S. Lysgaard, J. B. Maronsson, T. Maxson, T. Olsen, L. Pastewka, A. Peterson, C. Rostgaard, J. Schiøtz,

© 2025 The Author(s). Advanced Materials Interfaces published by Wiley-VCH GmbH

21967350, 2025, 13, Downloaded from https://advanced.onlinelibrary.wiley.com/doi/10.1002/admi.202500267 by Imperial College London, Wiley Online Library on [06/10/2025]. See the Terms and Conditions (https://onlinelibrary.wiley.com/terms-and-conditions) on Wiley Online Library for rules of use; OA articles are governed by the applicable Creative Commons License

O. Schütt, M. Strange, K. S. Thygesen, T. Vegge, et al., *J. Phys.: Condens. Matter* **2017**, *29*, 273002.
[38] H. J. C. Berendsen, J. R. Grigera, T. P. Straatsma, *J. Phys. Chem.* **1987**, *91*, 6269.
[39] F. Römer, A. Lervik, F. Bresme, *J. Chem. Phys.* **2012**, *137*, 074503.
[40] S. Kerisit, *Geochim. Cosmochim. Acta* **2011**, *75*, 2043.
[41] F. Leroy, S. Liu, J. Zhang, *J. Phys. Chem. C* **2015**, *119*, 28470.
[42] Z. Ge, D. G. Cahill, P. V. Braun, *Phys. Rev. Lett.* **2006**, *96*, 186101.
[43] N. Shenogina, R. Godawat, P. Keblinski, S. Garde, *Phys. Rev. Lett.* **2009**, *102*, 156101.
[44] D. Surblys, F. Müller-Plathe, T. Ohara, *J. Phys. Chem. A* **2022**, *126*, 5506.
[45] C. J. Fennell, J. D. Gezelter, *J. Chem. Phys.* **2006**, *124*, 234104.
[46] A. P. Thompson, H. M. Aktulga, R. Berger, D. S. Bolintineanu, W. M. Brown, P. S. Crozier, P. J. in 't Veld, A. Kohlmeyer, S. G. Moore, T. D. Nguyen, R. Shan, M. J. Stevens, J. Tranchida, C. Trott, S. J. Plimpton, *Comput. Phys. Commun.* **2022**, *271*, 108171.
[47] W. G. Hoover, *Phys. Rev. A* **1985**, *31*, 1695.
[48] S. Nosé, *Mol. Phys.* **1984**, *52*, 255.
[49] W. Shinoda, M. Shiga, M. Mikami, *Phys. Rev. B* **2004**, *69*, 134103.
[50] D. Becerra, J. H. Walther, H. A. Zambrano, *Nano Lett.* **2024**, *24*, 12054.
[51] Y. Guo, D. Surblys, H. Matsubara, Y. Kawagoe, T. Ohara, *J. Phys. Chem. C* **2020**, *124*, 27558.
[52] Z. Liang, M. Hu, *J. Appl. Phys.* **2018**, *123*, 191101.
[53] R. W. Hockney, J. W. Eastwood, *Computer simulation using particles*, CRC Press, **2021**.
[54] T. Schneider, E. Stoll, *Phys. Rev. B* **1978**, *17*, 1302.
[55] J. D. Olarte-Plata, F. Bresme, *Mol. Simul.* **2022**, *48*, 87.
[56] H. Matsubara, D. Surblys, T. Ohara, *Mol. Simul.* **2023**, *49*, 1365.
[57] J. D. Olarte-Plata, F. Bresme, *J. Chem. Phys.* **2022**, *156*, 204701.
[58] C. Bistafa, D. Surblys, H. Kusudo, Y. Yamaguchi, *J. Chem. Phys.* **2021**, *155*, 064703.
[59] K. Montazeri, M. J. A. Qomi, Y. Won, *ACS Appl. Mater. Interfaces* **2020**, *12*, 53416.
[60] D. Alexeev, J. Chen, J. H. Walther, K. P. Giapis, P. Angelikopoulos, P. Koumoutsakos, *Nano Lett.* **2015**, *15*, 5744.
[61] F. Bresme, E. Chacón, P. Tarazona, K. Tay, *Phys. Rev. Lett.* **2008**, *101*, 056102.
[62] J. A. Thomas, A. J. McGaughey, *J. Chem. Phys.* **2007**, *126*, 034707.
[63] M. Holz, S. R. Heil, A. Sacco, *Phys. Chem. Chem. Phys.* **2000**, *2*, 4740.
[64] P. B. Miranda, L. Xu, Y. R. Shen, M. Salmeron, *Phys. Rev. Lett.* **1998**, *81*, 5876.
[65] A. Soni, G. N. Patey, *J. Phys. Chem. C* **2021**, *125*, 10723.
[66] R. Aveyard, I. A. Haydon, *Trans. Faraday Soc.* **1965**, *61*, 2255.
[67] F. Bresme, J. Armstrong, *J. Chem. Phys.* **2014**, *140*, 016102.
[68] H. Sun, D. Surblys, H. Matsubara, T. Ohara, *Int. J. Heat Mass Transfer* **2023**, *208*, 124091.
[69] C. U. Gonzalez-Valle, B. Ramos-Alvarado, *ACS Appl. Nano Mater.* **2021**, *4*, 3821.
[70] A. Pesaran, S. Santhanagopalan, G. H. Kim, in *30th International Battery Seminar, National Renewable Energy Laboratory*, **2013**.
[71] J. Lan, B. Li, *Phys. Rev. B* **2006**, *74*, 214305.
[72] K. Zheng, F. Sun, J. Zhu, Y. Ma, X. Li, D. Tang, F. Wang, X. Wang, *ACS Nano* **2016**, *10*, 7792.
[73] X. Wei, T. Zhang, T. Luo, *ACS Appl. Mater. Interfaces* **2017**, *9*, 33740.
[74] S. A. Shavalier, J. D. Gezelter, *J. Chem. Inf. Model.* **2025**, *65*, 811.
[75] W. Chen, G. Nagayama, *Small Sci.* **2025**, *5*, 2400626.
[76] H. A. Patel, S. Garde, P. Keblinski, *Nano Lett.* **2005**, *5*, 2225.
[77] W. Yu, D. M. France, J. L. Routbort, S. U. Choi, *Heat Transfer Eng.* **2008**, *29*, 432.
[78] S. T. Huxtable, D. G. Cahill, S. Shenogin, L. Xue, R. Ozisik, P. Barone, M. Usrey, M. S. Strano, G. Siddons, M. Shim, P. Keblinski, *Nat. Mater.* **2003**, *2*, 731.
[79] A. S. Tascini, J. Armstrong, E. Chiavazzo, M. Fasano, *Phys. Chem. Chem. Phys.* **2017**, *19*, 3244.
[80] P. N. Acero, S. Mohr, M. Bernabei, C. Fernández, B. Domínguez, J. P. Ewen, *Langmuir* **2021**, *37*, 14582.
[81] S. E. Restrepo, M. C. P. van Eijk, J. P. Ewen, *Tribol. Int.* **2019**, *137*, 420.
[82] S. von Goeldel, T. Reichenbach, F. König, L. Mayrhofer, G. Moras, G. Jacobs, M. Moseler, *Tribology Letters* **2021**, *69*, 136.
[83] C. R. Wand, S. Gibbon, P. Visser, F. R. Siperstein, *Chem. - Eur. J.* **2022**, *28*, 202202483.
[84] A. J. Armstrong, R. F. G. Apóstolo, T. M. McCoy, F. J. Allen, J. Doutch, B. Cattoz, P. J. Dowding, R. Welbourn, A. Routh, P. J. Camp, *Nanoscale* **2024**, *16*, 1952.
[85] R. I. Taylor, R. Mainwaring, R. M. Mortier, *Proc. Inst. Mech. Eng., Part J* **2005**, *219*, 331.

© 2025 The Author(s). Advanced Materials Interfaces published by Wiley-VCH GmbH

21967350, 2025, 13, Downloaded from https://advanced.onlinelibrary.wiley.com/doi/10.1002/admi.202500267 by Imperial College London, Wiley Online Library on [06/10/2025]. See the Terms and Conditions (https://onlinelibrary.wiley.com/terms-and-conditions) on Wiley Online Library for rules of use; OA articles are governed by the applicable Creative Commons License